This is a preprint, the final version is subject to change, of the American Mineralogist (MSA)
Cite as Authors (Year) Title. American Mineralogist, in press.
(DOI will not work until issue is live.) DOI: http://dx.doi.org/10.2138/am.2014.4625

Revision 1

XAS Evidence for Ni Sequestration by Siderite in a Lateritic Ni-Deposit from New Caledonia.

Gabrielle Dublet[1,2]*, Farid Juillot[1,3], Guillaume Morin[1], Emmanuel Fritsch[1], Vincent Noel[1], Jessica Brest[1], and Gordon E. Brown Jr.[2,4]

[1]Institut de Minéralogie et de Physique des Milieux Condensés (IMPMC), UMR CNRS 7590, UR IRD 206, Université Pierre et Marie Curie (UPMC), Campus Jussieu, 75252, Paris Cedex 05, France

[2]Department of Geological & Environmental Sciences, Stanford University, Stanford CA 94305-2115, USA

[3] UFR STEP, Université Paris Diderot - IPGP, Bâtiment Lamarck, 75013 Paris, France

[4]Stanford Synchrotron Radiation Lightsource, 2575 Sand Hill Road, Menlo Park, California, 94025, USA

*Corresponding author: gdublet@stanford.edu

ABSTRACT

Mineralogical and spectroscopic analyses were conducted on a lateritic Ni-deposit from Southern New Caledonia. Results show that Ni is incorporated in siderite ($FeCO_3$) found between 37 m and 40 m depth in the laterite and saprolite units of the regolith. SEM-EDXS analyses of siderite-rich samples indicate that a significant amount of nickel can be hosted by this crystalline phase (~ 0.8 wt% NiO). Ni and Fe K-edge Extended X-ray Absorption Fine Structure (EXAFS) spectroscopic analyses of the siderite-rich samples from the regolith as well as comparison with synthetic Ni-bearing and Ni-free siderites demonstrate isomorphous substitution of Ni^{2+} for Fe^{2+} in the siderite structure. Linear Combination Fitting (LCF) of the Ni K-edge EXAFS data reveals that this Ni-bearing siderite species accounts for more than 90% of the total Ni pool (1 wt% NiO) in the siderite-rich horizons of the regolith. In addition, LCF analysis of the EXAFS spectra indicates that goethite and serpentine are the major Ni hosts in the upper horizons (laterite) and lower horizons (saprolite) of the regolith, respectively. Formation of siderite, an uncommon mineral species in such oxidized environments, is attributed to the development of swampy conditions in organic-rich lateritic materials that accumulated at the bottom of dolines. These results thus show the importance of siderite as a host for nickel in lateritic Ni deposits that have been affected by late hydromorphic and reducing conditions.

Keywords: siderite, XAS, nickel, laterite, speciation

INTRODUCTION

Siderite ($FeCO_3$) is a common carbonate mineral in sedimentary environments where it is considered as a diagenetic product (Postma 1981, 1982; Pye et al. 1990; Mozley 1989; Mozley and Wersin 1992; Ohmoto et al. 2004). Siderite is also classically found in wetland soils where it usually occurs as millimeter-scale spherulites known as sphaerosiderite (Ludvigson et al. 1998; Ufnar et al. 2001; 2004; White et al. 2001, 2005; Sheldon and Tabor 2009). Occurrences of pedogenic siderite with non-spherulitic morphologies have also been reported for poorly drained and swampy peat soils (McMillan and Schwertmann 1998; Driese et al. 2010). In most of these soil environments, siderite is considered to result from in situ reaction between dissolved carbon and ferrous iron after microbially mediated oxidation of organic matter and coupled reduction of Fe-oxides under reducing conditions (Ellwood et al. 1988; Mortimer et al. 1997; Mortimer and Coleman 1997; Frederickson et al. 1998). In addition to this classical route of formation, direct precipitation of siderite from the water column has also been proposed for evaporitic systems like in the Plio-Pleistocene section of the Black Sea (Rajan et al. 1996). Finally, in contrast with these ambient or low temperature reactions, a few occurrences of siderite have also been found associated with high-temperature metasomatic processes as in the Huttenberg siderite deposit (Carinthia, Austria; Bau and Moller 1992) and in the alteration halo of actinolite-bearing metabasic rocks in the Kalgoorlie area (Western Australia; White et al. 2003). In addition, non-biologically driven transformations of goethite or hematite to siderite have been studied at elevated temperatures with supercritical CO_2 and aqueous sulfide (Lammers et al. 2011; Murphy et al. 2011).

The routes of siderite formation thus generally involve reducing conditions, which suggests that precipitation of siderite in oxidizing lateritic environments should not be common. However, several occurrences of siderite in lateritic regoliths have been reported. For instance, this mineral species was found in a lignitic horizon in a buried laterite from the Late Cretaceous (Cenomanian) in southwestern Minnesota (Fritz and Toth 1997; Toth and Fritz 1997; Feng and Yapp 2009). Some siderite has also been found in association with rhodocrosite ($MnCO_3$) in the Ni-rich laterites from the swampy area of the Plaine des Lacs in the southern part of New Caledonia (Podwojewski and Bourdon 1996; Chen et al. 2004), and siderite occurrences have been reported in the Katjeli lateritic Ni-deposit in Albania and Greece associated with karstified Triassic limestones (Economou-Eliopoulos et al. 2003).

To our knowledge, isomorphous Ni^{2+} for Fe^{2+} substitution in siderite has not yet been directly reported for natural systems, although these two divalent ions have close effective ionic radii ($^{VI(HS)}Fe^{2+}$ = 0.78 Å and $^{VI}Ni^{2+}$ = 0.69 Å; Shannon 1976; Rimstidt et al. 1998). Several Ni-rich carbonate-hydroxide mineral species including nullaginite [$Ni_2(OH)_2CO_3$] (Nickel et al. 1979), otwayite [$(NiMg)_2(OH)_2CO_3 \bullet H_2O$], and eardleyite [$(Ni_6Al_2CO_3(OH)_{16} \bullet 4H_2O)$] have been identified in lateritic regoliths developed over disseminated metal sulfide deposits in ultramafic rocks from Western Australia (Nickel et al. 1977a, 1977b, 1977c; Butt and Nickel 1981), but no occurrence of Ni-bearing siderite was reported for these laterites. In mine tailings from Sardinia, selective chemical extraction data indicated that nickel is associated with various carbonates identified in the sulfide gangue where siderite was detected (Fanfani et al. 1997). However, the mineral species hosting Ni were not specified.

Based on extended x-ray absorption fine structure (EXAFS) spectroscopy, the present study reports direct spectroscopic evidence for isomorphic substitution of Ni^{2+} in siderite formed within a Ni-rich lateritic regolith from Southern New Caledonia. In addition, quantitative analysis of Ni speciation along this 43 m thick regolith profile shows the importance of this Ni-bearing species in this type of siderite-rich lateritic formation.

MATERIALS AND METHODS

Natural and synthetic samples. Natural samples studied were collected from a 43 m deep core drilled into the Goro lateritic Ni ores (New Caledonia) by the Vale NC company. The core samples are 50 cm to 1 m long sections, centered at specified depths and stored in ambient conditions. One half section of each core sample was dried at 105 °C during 12 to 24 hours, ground to powder and analyzed by ICP-AES. These powder samples were later analyzed by X-ray diffraction (XRD) and EXAFS spectroscopy. The second half of the sections of selected core samples was used to prepare hand-polished thin sections after impregnation in epoxy resin for scanning electron microscopy-energy dispersive x-ray spectroscopic (SEM-EDXS) analysis and electron probe microanalyses (EPMA).

Synthetic Ni-free and Ni-bearing siderite samples were prepared and served as model compounds for XRD and EXAFS analyses. These samples were synthesized in an anaerobic chamber with O_2-free milli-Q water previously sparged with N_2 for 40 min at 80 °C. For the Ni-free siderite, 5 mL of a 2 M $FeCl_2$ solution (filtered to 0.2 μm to

remove potential Fe-colloids) were mixed with 3 mL of a 2 M ascorbic acid solution. For the Ni-bearing siderite, nickel was introduced in this mixture by dissolving 117 mg of $NiCl_2.4H_2O$ (Ni/(Fe + Ni) = 5 mol%). For both syntheses, the resulting pH of this acidic solution was 2.5. An alkaline solution was then prepared by dissolving 6.3 g $NaHCO_3$ in 200 mL distilled and oxygen-free water. The acidic and alkaline solutions were then mixed together and the mixture slowly stirred for 1 h with pH stabilized at 7. At the end of this reaction time, a grayish to white precipitate of siderite was observed. In order to increase the crystallinity of this siderite, the suspension was poured into a glass bottle that was sealed and heated at 120 °C for 24 h. The suspension was then centrifuged at 5000 rpm under anaerobic conditions, washed with O_2-free milli-Q water, and vacuum-dried. The two synthetic siderite samples obtained following these protocols were checked by XRD and were found to be siderite (Fig. 1).

Mineralogical and chemical analyses. Mineralogical characterization of the natural and synthetic samples was performed by x-ray powder diffraction (XRD) with a Panalytical® X'pert Pro MPD diffractometer, using Co K-alpha radiation in order to minimize incident X-ray absorption by Fe. XRD data were recorded in continuous scan mode between 5 and 100 °2θ with 0.017 ° steps using an X'Celerator® detector and a total counting time of 4 to 6 hours per scan. Spatially resolved observations and analyses were performed by SEM-EDXS and EPMA. SEM observations and EDXS analyses were performed on C- or Au-coated thin sections using a Zeiss Ultra Field Emission Gun microscope equipped with a Bruker® Si-drift X-ray detector. Chemical distribution maps were performed using EDXS with a 15 kV electron beam collimated by a 60 µm circular aperture. Some SEM

observations in secondary electron mode were also performed on powder samples deposited on C tape. EPMA analyses were performed with a CAMECA SX50 equipped with four wavelength dispersive spectrometers (WDS) and operating at 15 kV and 10 nA at the Centre d'Analyse des Minéraux de Paris (CAMPARIS, Université Pierre et Marie Curie, Paris, France). Bulk concentrations of major (Si, Mg, Fe, Al, Ti, K, Ca, Na, Mn, and P) and trace (Ni, Co, Zn, Cu, Cr, and V) elements were determined by ICP-AES with a VARIAN 735-ES ICP Atomic Emission Spectrometer by the Australian Laboratory Services (ALS), subcontractors of VALE-NC (New Caledonia). The ALS used an analytical procedure, ME-ICP93 (Annexe 2), involving a decomposition with 10 times the powder weight of a lithium tetraborate (alkali fusion), and the dissolution of the resulting melts in dilute nitric acid. Total C concentrations were measured in a Shimazu TOC-L furnace at IRD, Nouméa.

Extended X-ray absorption fine structure (EXAFS) data collection. Ni K-edge EXAFS data were recorded on the high-flux wiggler beamline 11-2 at the Stanford Synchrotron Radiation Lightsource (SSRL, California, USA). Data were collected at 10 K using an Oxford Instruments® liquid helium cryostat in fluorescence-yield detection mode with a Canberra® high-throughput Ge 30-element solid-state array detector. The energy of the incoming x-ray beam was monitored with a Si(220) double-crystal monochromator over the 8.2 to 9.1 keV energy range. Fe K-edge EXAFS data for the synthetic siderite sample were recorded in transmission mode at 10 K on the bending magnet beamline SAMBA at the Source Optimisée de Lumière d'Energie Intermédiaire du Lure (SOLEIL, Saclay, France). The energy of the incoming x-ray beam was monitored in the 6.9 to 8.0 keV energy range with a Si(220) double-crystal

monochromator with dynamic sagittal focusing of the second crystal. For both Ni and Fe K-edge EXAFS data, energy was calibrated by setting the first inflection point of the absorption edge of Ni and Fe metal foils at 8333 eV and 7112 eV, respectively, with the foils placed after the second gas-filled ion chamber detector.

EXAFS data analysis. EXAFS spectra were averaged and background subtracted with the SIXPACK® code (Webb 2005). Fourier Transforms (FT) of the k^3-weighted spectra were calculated using the same code, after applying a Kaiser-Bessel window with a Bessel-weight of 2.5.

Ni and Fe K-edge EXAFS spectra of the synthetic Ni-free and Ni-bearing siderites were analyzed using a shell-by-shell procedure. For this procedure, the first four peaks of the FT of the k^3-weighted EXAFS from these two model compounds were back-transformed together by Fourier filtering to yield partial EXAFS spectra. Shell-by-shell fitting of these filtered $k^3\chi(k)$ functions was then performed in k-space with the plane-wave EXAFS formalism, using a Levenberg–Marquardt minimization algorithm. Theoretical phase-shift and amplitude backscattering functions employed in this shell-by-shell fitting procedure were calculated from the siderite structure (Graf 1961) with the curved-wave photo-electron scattering formalism using the ab initio Feff 8.10 code (Ankudinov et al. 1998) without using the self consistent potential option, for faster calculations.

Experimental EXAFS spectra of the natural regolith samples were analyzed using a linear combination fitting (LCF) procedure (e.g., Pickering et al. 1995). For this purpose, the spectra of the natural samples were first analyzed by Principal Component Analysis (PCA) using the SIXPACK® code (Webb 2005). The minimum number of

principal components necessary to fit all of the regolith sample spectra was chosen on the basis of the minimum value of the Factor Indicator Function of the PCA (Webb 2005; Table S1). The EXAFS spectra of model compounds that most likely represent the set of experimental EXAFS data were then selected according to a Target Transformation (TT) procedure (Malinowski 1978; Ndiba et al. 2008). This procedure was performed on a large set of model compound spectra reported in Dublet et al. (2012) in addition to the synthetic Ni-substituted siderite (see above). This set of model compounds spectra includes Ni K-edge EXAFS spectra of natural Ni-bearing phyllosilicates (serpentines, talcs, and smectite), natural mixed asbolane/lithiophorite, as well as synthetic Ni-bearing goethites. The choice of the most appropriate model compound spectra was based on the quality of the TT fits assessed using the Normalized Sum of Square Residual (NSSR: $\Sigma(k^3\chi_{target}-k^3\chi_{transform})^2/\Sigma(k^3\chi_{target})^2$) (Fig. S2; Table S1; Supporting Information). Finally, EXAFS spectra of the natural regolith samples were fit with linear combinations of the selected model compounds spectra, using the SIXPACK® code (Webb 2005). The accuracy of these fits is assumed to range between ± 25% and ± 5% of the stated values of each individual contribution, depending on the quality of the experimental data and on the occurrence of distinctive features in the data, based on past experience (Cancès et al. 2005; Manceau et al. 2000; Ostergren et al. 1999).

Cluster based calculations of the EXAFS spectra. Theoretical simulations of Ni K-edge EXAFS spectra were performed with the Feff 8.10 code (Ankudinov et al. 1998) on atom clusters of 9 Å in radius. For faster calculation, and because only the EXAFS region was used, neither self-consistent potential nor full-multiple scattering calculations were

performed in the XANES region. Two calculations were performed. The first one was done with Fe^{2+} as the central atom in a cluster having the siderite structure from Graf (1961) in order to calculate the Fe K-edge EXAFS spectrum of siderite. The second one was done by substituting Ni^{2+} for the central Fe^{2+} in the same cluster without changing interatomic distances, in order to calculate a Ni K-edge EXAFS spectrum of a Ni-substituted siderite. In each case, the whole set of single and multiple scattering paths up to 4-legs (total of 400 to 600 paths) was included in the EXAFS spectra calculation. The calculated EXAFS spectra were fit to the experimental ones by applying an overall Debye Waller factor, $\exp(-2k^2\sigma^2)$, a shift in the absorption edge energy, ΔE_0 (eV), and an amplitude reduction factor S_0^2, the values of which are given in Table 3.

RESULTS

Chemical and mineralogical composition of the lateritic regolith: localization of the siderite occurrence. The Fe_2O_3 vs. SiO_2 ratio is a good indicator for delineating lateritic and saprolitic materials in lateritic regolith soil sections (Fig. 2, Fandeur et al. 2009a, 2009b; Dublet et al. 2012). In the present study, high iron contents (> 70 wt% Fe_2O_3) and low silicon contents (< 2.7 wt% SiO_2) down to 30 m depth (Fig. 2, Table S3) indicate that the major part of the regolith (total thickness of 43 m) consists of lateritic material. This observation is in agreement with the aluminum content (5 to 7 wt% Al_2O_3) that is characteristic of lateritic horizons developed on Al-poor ultramafic rocks (< 1 wt% Al_2O_3). The texture of these lateritic materials is heterogeneous, with millimetric gravels

mixed with unconsolidated fine-textured lateritic matrix. Between 30 and 40 m depth, iron and aluminum concentrations tend to decrease irregularly, whereas silicon concentrations increase (from ~ 0 to ~ 40 wt%) (Fig. 2, Table S3). The chemical compositions in these units correspond to saprolitic materials more or less deeply weathered, tending to transition lateritic materials (11 to 65 wt% Fe_2O_3, 8 to 41 wt% SiO_2). Total carbon concentrations are significant in these units, with a maximum of 6.2 wt% at 36.1 m. Below 40 m depth, macroscopic observations and chemical concentrations of the core samples (< 10 wt% Fe_2O_3, ~ 40 wt% SiO_2) indicate the predominance of peridotitic bedrock (Fig. 2, Table S3). Compositional analyses indicate that the nickel concentration in the bedrock is low (0.4 wt% NiO; Fig. 2, Table S3), and close to values found elsewhere in the New Caledonian peridotite (Fandeur et al. 2009a, 2009b; Dublet et al. 2012). Ni concentrations are very variable in the saprolite, with an average of 1.2 wt% NiO that is rather low compared to values found elsewhere in the New Caledonian saprolitic Ni-ores (Fig. 2, Table S3; Fandeur et al. 2009a, 2009b; Dublet et al. 2012); however a narrow horizon (around 40 m depth) contains rather high nickel concentration (up to ~ 2 wt% NiO) (Fig. 2, Table S3). In the lateritic units, nickel concentration progressively decreases towards the surface, where it reaches a value of 0.6 wt% NiO (Fig. 2, Table S3).

XRD analysis indicates that siderite is found between 36.1 m and 40.3 m depth (i.e., in the 36.1 m, 36.9 m, 37.6 m, 38.6 m, and 40.3 m samples) and it is the dominant mineral in the lateritic (36.1 m) and saprolitic (37.6 m) samples (Fig. 2). Microscopic observations show that iron oxides and siderite occur mostly as aggregates of 10 to 100 μm diameter in the upper part of the siderite-rich horizon. Apart from the siderite-rich sample taken at 36.1 m, the lateritic samples between the surface and 36.9 m depth mainly consist of

goethite. They also contain traces of hematite near the surface and at 36.0 m, 36.9 m and 40.3 m (Fig. 2, Fig. S4), and small amounts of talc, serpentine and Mn-oxides (i.e., asbolane and lithiophorite) in below 30 m. Such a mineralogical composition is consistent with that usually found for lateritic samples from New Caledonia (Trescases 1979; Perrier et al. 2006a; Fandeur et al. 2009a, 2009b; Dublet et al. 2012). XRD data also indicate the occurrence of amphiboles (tremolite) at various depths in the regolith (Fig. 2). These mineral species are related to the original gabbroic veins reported for the ultramafic rocks of the Southern massifs of New Caledonia (Cluzel et al. 2006; Ulrich et al. 2010). Below 37 m, apart from the siderite-rich sample at 37.6 m, serpentine is the major mineral constituent in the 38.6 m and the 40.3 m samples, with minor contributions from olivine and pyroxenes, which corresponds to a saprolite composition. The occurrence of goethite, in particular in the 40.3 m sample, can be assigned to deeper levels of weathering in the irregular saprolite (Dublet et al. 2012). Finally, below 41 m depth, XRD patterns show the predominance of primary silicates (olivine, enstatite and serpentine), which is consistent with the mineralogy of the peridotitic bedrock (Trescases 1979; Perrier et al. 2006a; Fandeur et al. 2009a, 2009b; Dublet et al. 2012).

Crystal-chemistry of siderite in the New Caledonian regolith: Ni association with siderite. Rietveld refinement of the natural siderite XRD pattern (Fig. 1) indicates an average mean coherent domain size, MCD (111), of 100 ± 50 nm (Table 5). SEM observation of siderite grains in the 36 m depth sample shows that this crystalline phase can be found as sub-spherical grains of 100 to 200 μm in diameter aggregated in grape-like clusters (Fig. 3). Such a grape-like aggregation closely resembles the *coccoid* siderite

described by Driese et al. (2010) in alluvial clay soils from Tennessee (USA), although individual grains are of smaller size (20 μm) in these soils.

The spatial distribution of iron and carbon observed in this thin section by SEM-EDS shows high Fe concentrations around C-rich grains (Fig. 4). EPMA analyses performed on the C-rich grain yields an average sum of metal oxides of ~ 60 wt% (Table 1), which matches the value for siderite (62 wt% FeO). The average sum of metal oxides obtained for the Fe-rich matrix embedding the siderite grains is 76 wt% (Table 1), which can be assigned to goethite (81 wt% FeO), the major iron oxyhydroxide phase detected by XRD in this sample (Fig. 2). The MgO/SiO_2 ratio in this Fe-rich matrix is near 1.0 (Table 1), which suggests that Mg and Si are incorporated in serpentine that was also detected by XRD.

EPMA data show that siderite contains significant amounts of manganese (mean 3.90 wt% MnO) and lower amounts of magnesium (mean 0.96 wt% MgO), nickel (mean 0.86 wt% NiO), and cobalt (mean 0.40 wt% CoO) (Table 1). The structural formula of siderite determined from these EPMA analyses is $(Fe_{0.89}Mn_{0.06}Mg_{0.02}Ni_{0.01}Co_{0.01})CO_3$.

Ni K-edge EXAFS of synthetic Ni-bearing siderite. A synthetic Ni-bearing siderite sample was prepared as a model compound for analyzing EXAFS spectra of the natural samples studied. Results indicate that the Ni K-edge EXAFS spectrum of the synthetic Ni-bearing siderite is almost identical to the Fe K-edge EXAFS spectrum of the synthetic Ni-free siderite (Fig. 5A). This similarity indicates that the molecular environment of Ni^{2+} in the Ni-bearing siderite is similar to that of Fe^{2+} in Ni-free siderite. Results of the shell-by-shell analysis of both the Fe and Ni K-edges EXAFS spectra (Fig. 5, Table 2) are in excellent agreement with the siderite structure (Graf, 1961). This result is reinforced by

the good agreement obtained between the experimental EXAFS spectrum and theoretical ones calculated using a Ni-substituted siderite cluster with the ab initio Feff 8.10 code (Fig. 6, Table 3).

Ni K-edge EXAFS data for the New Caledonian regolith. From the bottom to the top of the regolith profile, four groups of samples can be distinguished, based on visual inspection of their Ni K-edge EXAFS spectra (Fig. 7) and on mineralogical analyses (Fig. 2). The first group consists of the deepest sample (43.0 m), which corresponds to the bedrock (Fig. 2). The EXAFS spectrum of this sample yields very weak features beyond the first-neighbor FT peak (Fig. 7). The second group consists of the 40.3 m sample, which belongs to the saprolite unit (Fig. 2). The EXAFS spectrum of this sample is similar to that of Ni-phyllosilicates (see Ni-rich serpentine in Fig. S2) and yields a second-neighbor contribution at a short distance ($R+\Delta \sim 2.8$ Å) uncorrected for phase-shift. The third group includes the 36.1 m and 37.6 m samples where the largest amount of siderite is observed by XRD (Fig. 2). These two samples exhibit sharp EXAFS spectra (Fig. 7) that closely resemble that of the Ni-bearing siderite (Fig. 5; Fig. 6). The last group corresponds to lateritic samples including the 36.9 m sample, and the samples collected at 32.7 m depth and above (i.e., 32.7 m, 28.7 m, 15.4 m, and 7.3 m), which are mainly composed of Fe- and Mn-oxides (Fig. 2). The EXAFS spectra of these samples are similar to that of Ni-bearing goethite (Fig. S2) with characteristic second- and third-neighbor peaks in the FT (Fig. 7).

Principal Component Analysis (PCA) suggests that the set of 9 EXAFS spectra from the regolith is composed of three to four principal components. Indeed, the IND parameter reaches its minimum value (i.e., 0.28) for the three or four first principal components,

which explain 84% or 88%, respectively, of the total variance of the system (Table S1; Supporting Information). This result is confirmed by the reconstruction of the set of 9 EXAFS spectra fit with the first, the two first, the three first, and the four first components (Fig. S1; Supporting Information). Target Transformation analysis indicates that a Ni-bearing forsterite, a Ni-poor serpentine from California, a Ni-rich serpentine from New Caledonia, a synthetic Ni-bearing goethite, a natural sample of mixed asbolane and lithiophorite (Asb/Lit), and a synthetic Ni-bearing siderite are the best candidates for the linear combination fits of the 9 EXAFS spectra from the natural samples (Fig. S2; Supporting Information).

For the 43.0 m sample, LCF yields 58% Ni-bearing forsterite and 42% Ni-poor serpentine (Fig. 7; Table 4). This result compares very well with the LCF results for the Ni K-edge EXAFS spectra from other bedrock samples from New Caledonia (Dublet et al. 2012). The 40.3 m sample EXAFS spectrum is fit with a mixture of 52% Ni-rich serpentine and 48% Ni-bearing goethite (Fig. 7; Table 4), which also compares very well with EXAFS results reported for other saprolitic samples from New Caledonia (Dublet et al. 2012). EXAFS spectra of the lateritic samples at depths of 28.7 m, 15.4 m and 7.3 m are well fit with 80% Ni-bearing goethite and 18 to 25% Ni-bearing Mn-oxides (Fig. 7; Table 4). This latter result is in good agreement with the reported speciation of nickel in lateritic units of the Ni deposits from West Africa (Manceau et al. 2000) and New Caledonia (Dublet et al. 2012). EXAFS spectra of the 32.7 m and 36.9 m samples are fit with 66% to 68% Ni-bearing goethite, 19% to 23% Ni-bearing Mn-oxides, and 9% to 15% of Ni-bearing serpentine, which corresponds to Ni-speciation in the transition laterite unit of New Caledonian Ni-deposits (Dublet et al. 2012). Traces of siderite were detected by XRD in these two latter samples (Fig. 2), but including a Ni-bearing siderite

component in the LC fit did not significantly improve the fit quality. The presence of such a component can not, however, be ruled out, given that the detection limit of minor EXAFS components can be as high as 10% of the total absorber concentration (Cancès et al. 2005; Ostergren et al. 1999). LCF indicates that Ni-speciation in the two siderite-rich samples, i.e., at depths of 37.6 m and 36.1 m, consist of 52% Ni-bearing siderite + 48% Ni-rich serpentine, and 88% siderite + 12% Ni-rich serpentine, respectively (Fig. 7; Table 4). These results thus yield the first direct evidence for nickel incorporation in siderite in a natural environment. They also indicate that siderite can be an important host for nickel in lateritic regoliths, under certain weathering conditions, which are discussed below.

DISCUSSION

Isomorphous substitution of Ni^{2+} for Fe^{2+}. Rietveld analysis of the XRD powder patterns yielded similar cell parameters for the synthetic Ni-free siderite, the Ni-bearing siderite and the natural Ni-bearing siderite, as those reported for the siderite structure refined by Graf (1961) (Table 5). Indeed, the Ni concentrations in the natural and synthetic siderite samples here are too low to detect any change in unit cell parameters at the scale of the bulk crystals. According to the effective ionic radii determined by Shannon (1976), the Fe-O and Ni-O inter-atomic distances should be 2.18 Å and 2.09 Å, respectively. Assuming Vegard's law, the Ni substitution level of 5 mol% in the synthetic samples studied should thus result in a shortening of 0.2% of the unit cell parameters. This variation is of the same order of magnitude as the accuracy of the unit cell parameters determined in the present Rietveld refinement (± 0.3% relative at best; Table

5). The Ni substitution level is even lower in the natural Ni-bearing siderite. However, based on the shell-by-shell fits of the EXAFS spectra, the Ni-O (first-neighbor) distance (2.08 ± 0.01 Å) for the synthetic Ni-bearing siderite is slightly shorter than the Fe-O (first-neighbor) distance (2.13 ± 0.01 Å) for the Ni-free one (Table 4). This EXAFS result suggests local relaxation of the first coordination sphere around the substituting Ni^{2+} ion, as expected from the difference in effective ionic radii values of $^{VI,HS}Fe^{2+}$ (0.78 Å) and $^{VI}Ni^{2+}$ (0.69 Å) (Shannon, 1976). Despite this short-range relaxation, an acceptable agreement is found between the experimental EXAFS spectra and the spectra calculated for a cluster where Ni^{2+} substitutes for Fe^{3+} in siderite without applying a scaling factor to the unit cell parameters (Fig. 6). This latter agreement is supported by the fact that the distances corresponding to the second and the third coordination shells around Ni^{2+} are found to be similar in the Ni-free or Ni-bearing siderites, according to the shell-by-shell fit results (Table 2). Therefore, structural relaxation around Ni^{2+} in the siderite structure appears to be limited to the first coordination shell. In addition, the FT amplitudes corresponding to second and third shells of the synthetic Ni-bearing siderite are lower than for the Ni-free siderite, which is related to the slight differences between the Ni and Fe K-edge spectra of these samples, which can be observed especially between 4 and 6 $Å^{-1}$ and ~ 8 $Å^{-1}$. Such differences could be due to disorder linked to the accommodation of short-range strain caused by the Ni^{2+} for Fe^{2+} substitution.

Origin of siderite in the lateritic regolith. As mentioned in the introduction, it is widely thought that the precipitation of siderite in surface environments is an ambient-temperature process driven by microbial activity (Ellwood et al. 1988; Coleman et al. 1993; Mortimer et al. 1997; Mortimer and Coleman 1997; Konhauser 1998). In their study of lateritic samples from the Plaine des Lacs in the Southern massifs of New

Caledonia, Podwojewski and Bourdon (1996) reported the co-occurrence of siderite with rhodocrosite. These authors proposed that these minerals formed at ambient temperature under reducing conditions in soils rich in organic matter and with a high partial pressure of CO_2. A related formation pathway can be proposed for Ni-bearing siderite in the lateritic regolith investigated in the present study, since it is located only a few kilometers from the area studied by Podwojewski and Bourdon (1996). In addition, the grape-like aggregate morphology of the sub-spherical siderite grains observed by SEM (Fig. 3) is also in agreement with a pedogenic origin, as already reported by Driese et al. (2010) for alluvial clay soils from Tennessee (USA). Finally, the chemical composition of the siderite in the investigated regolith can be linked to the one of continental waters. Indeed, Mozley (1989) indicated that the purity of continental siderite is usually higher than that of marine siderite, which can contain up to 41 mol% Mg and 15 mol% Ca substituting for Fe. Mozley (1989) also reported that continental siderite samples usually show a higher Mn content than marine ones. The results of EPMA performed on the siderite grains collected from the regolith in the present study indicate a lack of Ca, very low amounts of Mg (0.6 mol%), and significant amounts of Mn (1.4 mol%) (Table 1). All of these findings strongly suggest that the siderite observed in the regolith in the present study is of pedogenic origin (i.e., formed during surface weathering) and that it formed from continental waters rather than seawater.

Possible implications for geomorphologic and/or hydrogeologic processes. The mineralogical composition and the macroscopic features of the discordant siderite-containing horizons of the regolith can enhance our understanding of the formation conditions of this mineral species within a lateritic environment. First, the saprolitic units

are very thin relatively to the very thick lateritic units above, in comparison to other lateritic regoliths described elsewhere (Trescases 1979; Dublet et al. 2012), which suggests the contribution of allochtonous lateritic materials. In addition, XRD detection of significant amounts of hematite in a deep sample collected at 36.0 m, which is just above the sample most enriched in siderite (i.e., 36.1 m depth; Fig. 2; Fig. S4), is surprising in these ultramafic lateritic systems from New Caledonia, where goethite is generally the major Fe-oxide. Indeed, in these lateritic covers, hematite often occurs in the topmost part of the laterite (Trescases 1979; Perrier et al. 2006a, 2006b; Traore et al. 2008; Fandeur et al. 2009a, 2009b; Dublet et al. 2012). The presence of hematite in this zone is related to drier conditions at the top of the laterite that result from the free drainage of water and/or to repeated bush fires (Ruan and Gilkes 1995; Wells et al. 2006; Perrier et al. 2006b). In contrast, we interpret the occurrence of hematite at such great depths (below 30 m) in the New Caledonian laterites as a signature of buried material originating from the topmost part of the surrounding lateritic massifs. This interpretation is in agreement with the optical microscopy observation of 10 to 200 μm diameter nodules of Fe/Mn-oxides in the 36 m depth sample, whereas such nodules are generally observed in the top horizons of laterites. It is also in agreement with macroscopic observations of red colored heterogeneities of millimetric gravels down to at least 20 m depth in the laterite. This laterite can thus be considered as reworked, which is fully consistent with its location in soil collapse zones, as indicated by the geological map of the Southern part of New Caledonia (Sevin et al. 2012). These soil collapses are related to the karstic conditions encountered in these deeply weathered ultramafic formations (Genna et al. 2005). Based on this hypothesis, the horizons between 40.3 and 36.1 m depth that contain siderite are

likely to comprise a paelosurface that corresponds to the bottom of a doline. Indeed, as already proposed by Podwojewski and Bourdon (1996), these topographical local depressions are favorable to the development of swampy, reducing conditions contrasting with the normally oxidizing environment of laterites. Under such reducing conditions, bacterial oxidation of accumulated organic matter coupled with reductive dissolution of Fe-oxides provide large amounts of dissolved CO_2 and ferrous iron that are necessary for siderite formation (Ellwood et al. 1988; Coleman et al. 1993; Mortimer et al. 1997; Frederickson et al. 1998; Zachara et al. 1998). In such a model, siderite would have formed in the horizons between 40.3 and 36.1 m depth after progressive accumulation of both colluvial lateritic material and organic matter at the bottom of the doline. The absence of siderite in the horizons above 36 m depth would indicate that these episodes of swampy conditions have been followed by other environmental conditions, such as a major tectonic uplift accompanied by a massive accumulation of lateritic material (Lagabrielle et al. 2005), or a drop of the water-table (Genna et al. 2005; Chevillotte et al. 2006) or a combination of both.

SEM observation of samples from the top of the siderite horizon shows that some siderite grains have undergone transformation into iron oxides, which appear as fillings in siderite cracks (Fig. 3). Such transformations can be due to partial re-oxidation either after the drill core sampling or during natural redox cycles, for example by a lowering of the water table level, or both. This type of cyclic evolution of iron oxides/siderite is common in continental redox boundaries (McMillan and Schwertmann 1998).

Proposed pathway for Ni/Mn-bearing siderites in the New Caledonian laterite. As discussed in the paragraph above, siderite could have formed after reductive dissolution of

Fe(III)-oxides during hydromorphic episodes. We have shown that this mineral phase contains significant amounts of Mn, Mg, Ni, and Co (Table 1). Although Mn and Mg are commonly hosted by siderite (Mozley 1989), the association of Ni and Co with natural siderite has been only rarely reported (Fanfani et al. 1997). Goethite is the main Ni-host in the lateritic unit of the regolith (Table 4), as already reported for Ni-deposits from other localities in New Caledonia (Dublet et al. 2012), and this phase contains significant amounts of Mn and Co (Table 1). Hence, dissolution of goethite could have resulted in the release of significant amounts of Ni, Mn, and Co that would have been subsequently sequestered in siderite (Kukkadapu et al. 2001; Zachara et al. 2001). In addition, Podwojevski and Bourdon (1996) reported the formation of rhodochrosite in lake sediments related to a similar New Caledonian laterite deposit, which suggests that reductive dissolution of Mn-oxides could have also contributed as a source of Ni and Mn impurities in siderite. Indeed, Fandeur et al. (2009b) showed that $Mn^{(III,IV)}$-oxides occurring in laterites from New Caledonia contain significant amounts of nickel. The (bio)reduction of such Mn oxides coupled with organic matter oxidation (Lovley and Phillips 1988; Lovley 2004) could have also released Ni and Mn as well as CO_2 and contributed to the formation of Ni/Mn-rich siderites in the New Caledonian laterites. We thus conclude that the Ni/Mn-bearing siderite in the New Caledonian laterites could have formed from the bioreduction of Ni/Mn-bearing goethite - and Mn-oxides - at the bottom of an ancient doline that was later buried under about 30 meters of colluvial lateritic materials.

ACKNOWLEDGMENTS

This work was supported by the Centre National de Recherche Technologique Nickel et son Environnement (CNRT) in Noumea (New Caledonia). CNRT is a Public Interest Group funded by the French and New Caledonian authorities and research organizations, as well as by international mining companies, for promoting local research programs in the field of sustainable mining of geological resources. The technical staffs at the SSRL (Stanford, USA) and SOLEIL (Saclay, France) Synchrotron Facilities are acknowledged for providing good beam conditions during EXAFS measurements. Portions of this research were carried out at the Stanford Synchrotron Radiation Lightsource, a national user facility operated by Stanford University on behalf of the U.S. Department of Energy, Office of Basic Energy Sciences. The authors thank Associate Editor Dr. Alejandro Fernandez-Martinez for fruitful comments upon handling of this manuscript, and Dr. Martin Wells, as well as two anonymous reviewers, for improving its quality.

REFERENCES

Ankudinov, A.L., Ravel B., Rehr, J.J. and Conradson, S.D. (1998) Real-space multiple-scattering calculation and interpretation of X-ray-absorption near-edge structure. *Physical Reviews* B 58, 7565–7576.

Bau, M. and Moller, P. (1992) Rare-earth element fractionation in metamorphogenic hydrothermal calcite, magnesite and siderite. *Mineralogy and Petrology*, 45, 231-246.

Butt, C.R.M. and Nickel, E.H. (1981) Mineralogy and geochemistry of the weathering of the disseminated sulfide deposit at Mt Keith, Western Australia. *Economic Geology*, 76, 1736-1751.

Cancès, B., Juillot, F., Morin, G., Laperche, V., Alvarez, L., Proux, O., Hazemann, J.L., Brown, G.E. Jr., and Calas, G. (2005) XAS Evidence of As(V) Association with Iron Oxyhydroxides in a Contaminated Soil at a Former Arsenical Pesticide Processing Plant. *Environmental Science & Technology,* 39, 9398-9405.

Chen, T.T., Dutrizac, J.E., Krause, E. and Osborne, R. (2004) Mineralogical characterization of nickel laterites from New Caledonia and Indonesia. *International Laterite Nickel Symposium-2004*, 79-99.

Chevillotte, V., Chardon, D., Beauvais, A., Maurizot, P. and Colin, F. (2006) Long-term tropical morphogenesis of New Caledonia (Southwest Pacific): Importance of positive epeirogeny and climate change. *Geomorphology,* 81, 361-375

Cluzel, D., Meffre, S., Maurizot, P. and Crawford, A.J. (2006) Earliest Eocene (53 Ma) convergence in the Southwest Pacific: evidence from pre-obduction dikes in the ophiolite of New Caledonia. *Terra Nova*, 18, 395-402.

Coleman, M.L., Hedrick, D.B., Lovley, D.R., White, D.C. and Pye, K. (1993) Reduction of Fe(III) in sediments by sulfate-reducing bacteria. *Nature*, 361, 436-438.

Driese, S.G., Ludvigson, G.A., Roberts, J.A., Fowle, D.A., Gonzalez, L.A., Smith, J.J., Vulaya, V.M. and McKay, L.D. (2010) Micromorphology and stable-isotope geochemistry of historical pedogenic siderite formed in PAH-contaminated alluvial clay sols, Tennessee, USA. *Journal of Sedimentary Research*, 80, 943-954.

Dublet, G., Juillot, F., Morin, G., Fritsch, E., Fandeur, D., Ona-Nguema, G. and Brown, G.E. Jr. (2012) Ni speciation in a New Caledonian lateritic regolith: A quantitative X-ray absorption spectroscopy investigation. *Geochimica et Cosmochimica Acta,* 95, 119–133.

Economou-Eliopoulos, M., Laskou, M., Tashko, A. and Eliopoulos, D.G. (2003) Mineralogical and geochemical features of the Katjeli Fe-Ni-laterite deposit, Pogradec massif. Albania. *Mineral Exploration and Sustainable Development*, 1 & 2, 73-76.

Ellwood, B.B., Chrzanowski, T.H., Hrouda, F., Long, G.J. and Buhl, M.L. (1988) Siderite formation in anoxic deep-sea sediments – A synergetic bacterially controlled process with important implications in paleomagnetism. *Geology*, 16, 980-982.

Fandeur, D., Juillot, F., Morin, G., Olivi, L., Cognigni, A., Ambrosi, J.-P., Guyot, F. and Fritsch, E. (2009a) Synchrotron-based speciation of chromium in an Oxisol from New Caledonia: importance of secondary Fe-oxyhydroxides. *American Mineralogist,* 94(5–6), 710–719.

Fandeur, D., Juillot, F., Morin, G., Olivi, L., Cognigni, A., Webb, S.M., Ambrosi, J.-P., Fritsch, E., Guyot, F. and Brown, G.E. Jr. (2009b) XANES evidence for oxidation of Cr(III) to Cr(VI) by Mn-oxides in a lateritic regolith developed on serpentinized ultramafic rocks of New Caledonia. *Environmental Science & Technol*ogy, 43(19), 7384–7390.

Fanfani, L., Zuddas, P., and Chessa, A. (1997) Heavy metals speciation analysis as a tool

for studying mine tailings weathering. *Journal of Geochemical Exploration,* 58, 241-248.

Feng, W. and Yapp, C.J. (2009) Paleoenvironmental implications of concentration and $^{13}C/^{12}C$ ratios of $Fe(CO_3)OH$ in goethite from a mid-latitude Cenomanian laterite in southwestern Minnesota. *Geochimica et Cosmochimica Acta*, 73, 2559–2580.

Frederickson, J.K., Zachara, J.M., Kennedy, D.W., Dong, H., Onstott, T.C., Hinman, N.W. and Li, S.M. (1998) Biogenic iron mineralization accompanying the dissimilatory reduction of hydrous ferric oxide by a groundwater bacterium. *Geochimica et Cosmochimica Acta*, 62, 3239-3257.

Fritz, S.J. and Toth, T.A. (1997) An Fe-berthierine from a Cretaceous Laterite: part 2. Estimation of Eh, pH and pCO_2 conditions of formation. *Clays and Clay Minerals,* 45, 580–586.

Genna, A., Maurizot, P., Lafoy, Y. and Augé, T. (2005) Contrôle karstique de minéralisations nickellières de Nouvelle-Calédonie. *Comptes Rendus Geoscience,* 337, 367–374.

Graf, D.L. (1961) Crystallographic tables for the rhombohedral carbonates. *American Mineralogist*, 46, 1283-1316

Konhauser, K.O. (1998) Diversity of bacterial iron mineralization. *Earth Science Reviews*, 43, 91-121.

Kukkadapu, R.K., Zachara, J.M., Smith, S.C., Frederickson, J.K. and Liu, C. (2001) Dissimilatory bacterial reduction of Al-substituted goethite in subsurface sediments. *Geochimica et Cosmochimica Acta*, 65, 2913-2924.

Lagabrielle, Y., Maurizot, P., Lafoyc, Y., Cabioch, G., Pelletier, B., Regnier, M., Wabeteg, I. and Calmanth, S. (2005). Post-Eocene extensional tectonics in Southern

New Caledonia (SW Pacific): Insights from onshore fault analysis and offshore seismic data. *Tectonophysics*, 403, 1-28.

Lammers, K., Murphy, R., Riendeau, A., Smirnov, A., Schoonen, M.A.A. and Strongin, D.R. (2011) CO_2 Sequestration through Mineral Carbonation of Iron Oxyhydroxides. *Environmental Science & Technology,* 45, 10422–10428

Lovley, D.R. (2004) Dissimilatory Fe(III) and Mn(IV) reduction. *Advances in Microbial Physiology*, 49, 219-286.

Lovley, D.R. and Phillips, E.J.P. (1988) Novel mode of microbial energy metabolism : Organic carbon oxidation coupled to dissimilatory reduction of iron or manganese. *Applied and Environmental Microbiol*ogy, 54, 1472-1480.

Ludvigson, G.A., Gonzalez, L.A., Metzger, R.A., Witzke, B.J., Brenner, R.L., Murillo, A.P. and White, T.S. (1998) Meteoric sphaerosiderite lines and their use for paleohydrology and paleoclimatology. *Geology*, 26, 1039-1042.

Malinowski, E.R. (1978) Theory of error for target factor analysis with applications to mass spectrometry and nuclear magnetic resonance spectrometry. *Analytica Chimica Acta* 103, 339–354.

Manceau, A., Schlegel, M.L., Musso, M., Sole, V.A., Gauthier, C., Petit, P.E., and Trolard, F. (2000) Crystal chemistry of trace elements in natural and synthetic goethite. *Geochimica et Cosmochimica Acta,* 64, 3643-3661.

McMillan, S.G. and Schwertmann, U. (1998) Morphological and genetic relations between siderite, calcite and goethite in Low Moor Peat from southern Germany. *European Journal of Soil Science*, 49, 283-293

Mortimer, R.J.G. and Coleman, M.L. (1997) Microbial influence on the oxygen isotopic composition of diagenetic siderite. *Geochimica et Cosmochimica Acta*, 61, 1705-

1711.

Mortimer, R.J.G., Coleman, M.L. and Rae, J.E. (1997) Effect of bacteria on the elemental composition of early diagenetic siderite: implications for palaeoenvironmental interpretations. *Sedimentology*, 44, 759-765.

Mozley, P.S. (1989) Relation between depositional environment and the elemental composition of early diagenetic siderite. *Geology*, 17, 704-706.

Mozley, P.S. and Wersin, P. (1992) Isotopic composition of siderite as an indicator of depositional environment. *Geology*, 9, 817-820.

Murphy, R., Lammers, K., Smirnov, A., Schoonen, M.A.A., and Strongin, D.R. (2011) Hematite reactivity with supercritical CO_2 and aqueous sulfide. *Chemical Geology,* 283, 210-217.

Ndiba, P., Axe, L. and Boonfueng, T. (2008) Heavy metal immobilization through phosphate and thermal treatment of dredged sediments. *Environmental Science & Technology,* 42, 920–926.

Nickel, E.H., Robinson, B.W., Davis, C.E.S. and MacDonald, R.D. (1977a) Otwayite, a new nickel mineral from Western Australia. *American Mineralogist*, 62, 999-100.

Nickel, E.H., Davis, C.E.S., Bussell, M., Bridge, P.J., Dunn, J.G. and MacDonald, R.D. (1977b) Eardleyite as a product of supergene alteration of nickel sulfides in Western Australia. *American Mineralogist*, 62, 449-457.

Nickel, E.H., Allchurch, P.D., Mason, M.G. and Wilmshurst, J.R. (1977c) Supergene alteration at perseverance nickel deposit, Agnew, Western Australia. *Economic Geology*, 72, 184-203.

Nickel, E.H., Hallberg, J.A. and Halligan, R. (1979) Unusual nickel mineralisations at Nullagine. Western Australia. *Journal of the Geological Society of Australia*, 26, Issue 1-2.

Ohmoto, H., Watanabe, Y. and Kumazawa, K. (2004) Evidence from massive siderite beds for a CO_2-rich atmosphere before, 1.8 billion years ago. *Nature*, 429, 395-399.

Ostergren, J.D., Brown, G.E. Jr., Parks, G.A., and Tingle, T.N. (1999). Quantitative Speciation of Lead in Selected Mine Tailings from Leadville, CO. *Environmental Science & Technology,* 33, 1627-1636.

Perrier, N., Ambrosi, J.-P., Colin, F. and Gilkes, R.J. (2006a) Biogeochemistry of a regolith: The New Caledonian Koniambo ultramafic massif. *Journal of Geochemical Exploration*, 88(1–3), 54–58.

Perrier, N., Gilkes, R.J. and Colin, F. (2006b) Heating Fe oxide-rich soils increases the dissolution rate of metals. *Clays and Clay Minerals*, 54, 165-175.

Pickering, I.J., Brown, G.E. Jr., Tokunaga, T.K. (1995) Quantitative speciation of selenium in soils using x-ray absorption spectroscopy. *Environmental Science & Technology,* 29, 2456-2459.

Podwojewski, P. and Bourdon, E. (1996) The induration process of goethitic oxisols on peridotites in New Caledonia: a singular plinthite-type process of induration. *Comptes Rendus de l'Académie des Sciences de Paris*, 322, II a, 453-459.

Postma D. (1981) Formation of siderite and vivianite and the pore-water composition of a recent bog sediment in Denmark. *Chemical Geology*, 31, 225-244.

Postma, D. (1982) Pyrite and siderite formation in brackish and fresh-water swamp sediments. *American Journal of Science*, 282, 1151-1183.

Pye, K., Dickson, J.A.D., Schiavon, N., Coleman, M.L. and Cox, M. (1990) Formation of

siderite - Mg-calcite - iron sulfide concretions in intertidal mars hand sandflat sediments, North-Northfolk, England. *Sedimentology*, 37, 325-343.

Rajan, S., Mackenzie, F.T. and Glenn, C.R. (1996) A thermodynamic model for water column precipitation of siderite in the Plio-Pleistocene Black Se. *American Journal of Science,* 296, 506-548.

Rimstidt, D., Balog, A. and Webb, J., (1998) Distribution of trace elements between carbonate minerals and aqueous solutions, *Geochimica et Cosmochimica Acta*, 62(11) 1851–1863

Ruan, H.D. and Gilkes, R.J. (1995) Dehydroxylation of aluminous goethite: unit cell dimensions, crystal size and surface area. *Clays and Clay Minerals*, 43, 196-211.

Sevin, B., Maurizot, P. and Vendé-Leclerc, M. (2012) *Carte géologique du Grand Sud de Nouvelle-Calédonie au 1/50000. 1ère edition.* BRGM, Service géologique de Nouvelle-Calédonie.

Shannon, R.D. (1976) Revised Effective Ionic Radii and Systematic Studies of Interatomic Distances in Halides and Chalcogenides. *Acta Crystallographica,* A32, 751.

Sheldon, N.D. and Tabor, N.J. (2009) Quantitative paleoenvironmental and paleoclimatic reconstruction using paleosols. *Earth-Science Reviews*, 95, 1–52.

Toth, T.A. and Fritz, S.J. (1997) An Fe-berthierine from a Cretaceous Laterite: part 1. Characterization. *Clays and Clay Minerals,* 45, 564–579.

Traore, D., Beauvais, A., Chabaux, F., Peiffert, C., Parisot, J.-C., Ambrosi, J.-P., and Colin, F. (2008) Chemical and physical transfers in an ultramafic rock weathering profile: Part 1. Supergene dissolution of Pt-bearing chromite. *American Mineralogist,* 93, 22-30.

Trescases, J.-J. (1979) Remplacement progressif des silicates par les hydroxydes de fer et de nickel dans les profils d'altération tropicale des rohes ultrabasiques. Accumulation résiduelle et épigénie. *Sciences Geologiques Bulletin,* 32, 7p.

Ufnar, D.F., Gonzales, L.A., Ludvigson, G.A., Brenner, R.L. and Witzke, B.J. (2001) Stratigraphic implications of meteoric sphaerosiderite $\delta^{18}O$ values in paleosols of the Cretaceous (Albian) Boulder Creek Formation, NE British Columbia Foothills, Canada. *Journal of Sedimentary Research*, 71, 1017-1028.

Ufnar, D.F., Gonzalez, L.A., Luvigson, G.A., Brenner, R.L. and Witzke B.J. (2004) Diagenetic overprinting of the sphaerosiderite palaeoclimate proxy: are records of pedogenic groundwater $\delta^{18}O$ values preserved? *Sedimentology*, 51, 127–144

Ulrich, M., Picard, C., Guillot, S., Chauvel, C., Cluzel, D. and Meffre, S. (2010) Multiple melting stages and refertilization as indicators for ridge to subduction formation: The New Caledonia ophiolite. *Lithos*, 115, 223-236.

Webb, S.M., (2005). SIXpack: a graphical user interface for XAS analysis using IFEFFIT. *Physica Scripta,* T115:1011-1014.

Wells, M.A., Fitzpatrick R.W. and Gilkes R.J. (2006) Thermal and mineral properties of Al-, Cr-, Mn-, Ni- and Ti-substituted goethite. *Clays and Clay Minerals*, 54, 176-194.

White, T., Gonzales, L., Ludvigson, G. and Poulsen, C. (2001) Middle Cretaceous greenhouse hydrologic cycle of North America. *Geology*, 29, 363-366.

White, R.W., Powell, R. and Phillips, G.N. (2003) A mineral equilibria study of the hydrothermal alteration in mafic greenschist facies rocks at Kalgoorlie, Western Australia. *Journal of Metamorphic Geology*, 21, 455-468.

White, T., Witzke, B., Ludvigson, G. and Brenner, R. (2005) Distinguishing base-level change and climate signals in a cretaceous alluvial sequence. *Geology*, 33, 13-16.

Zachara, J.M., Fredrickson, J.K., Li, S.M., Kennedy, D.W., Smith, S.C. and Gassman, P.L. (1998) Bacterial reduction of crystalline Fe^{3+} oxides in single phase suspensions and subsurface materials. *American Mineralogist*, 83, 1426-1443.

Zachara, J.M., Fredrickson, J.K., Smith, S.C. and Gassman, P.L. (2001) Solubilization of Fe(III) oxide-bound trace metals by a dissimilatory Fe(III) reducing bacterium. *Geochimica et Cosmochimica Acta*, 65, 75-93.

FIGURES CAPTIONS

Figure 1. Experimental (black lines) and Rietveld refined (red lines) XRD patterns of the synthetic Ni-free and Ni-bearing siderites. srp: serpentine, en: enstatite. The "K" at low angles above the XRD pattern of the Ni-bearing siderite indicates a diffraction peak from the Kapton foil of the anoxic cell and the label "s.h." indicates scattering from the sample holder.

Figure 2. SiO_2, Fe_2O_3, NiO, and Al_2O_3 concentrations and XRD patterns of the samples collected as a function of depth in the regolith. (a: asbolane; l: lithiophorite; am: amphibole; srp: serpentine; tlc: talc; gt: goethite; hem: hematite; chr: chromite; sid: siderite; qtz: quartz). XRD patterns of the samples containing siderite are shown in black and occur at depths from 36.1 m to 40.3 m.

Figure 3. SEM secondary electron image of siderite grains about 200 μm in diameter (dark gray) aggregated in grape-like clusters in the sample collected at 36 m depth in the regolith. The pale gray color corresponds to goethite. The red square corresponds to the location of the compositional analyses in Figure 4.

Figure 4. SEM-EDX chemical distribution of carbon, iron, nickel, and silicon showing siderite (high carbon content) embedded in a matrix of Fe-oxides and Mg-silicates in the sample collected at 36.1 m depth in the regolith. The bold white line shows the location of the EPMA analyzes reported in Tables 1 and S2.

Figure 5. Comparison of the Fe and Ni K-edge EXAFS data of the Ni-free and Ni-bearing synthetic samples, respectively. The (a) panel shows the background-subtracted, k^3-weighted EXAFS spectra, and the (b) panel shows fits of the Fourier-filtered backtransformed EXAFS spectra over the R-range 0-4.5 Å. Panel (c) shows the shell-by-shell fit within the 0-4.5 Å R-range, uncorrected for phase-shift. Black and red lines correspond to experimental data and shell-by-shell fits, respectively.

Figure 6. (Left panels) Fits of the Fe and Ni K-edge experimental EXAFS spectra of the synthetic Ni-free and Ni-bearing siderites (black lines) with the Feff-calculated EXAFS spectra (red lines) obtained by including the parameters σ, S_0^2 and ΔE_O; (Right panels) the corresponding Fourier Transforms of the EXAFS spectra.

Figure 7. Ni K-edge (a) EXAFS spectra and corresponding (b) FT (real part), and (c) FT (imaginary part) for samples collected at various depths in the lateritic regolith. Black lines correspond to experimental data and red lines correspond to linear combination least squares fits (see Table 4 for quantitative results).

TABLES CAPTIONS

Table 1. EPMA analyses at the interface between the siderite grain and its surrounding matrix of Fe-oxides and Mg-silicates shown on Figure 3.

Table 2. Results of shell-by-shell fit of the Ni and Fe K-edges EXAFS spectra for the

synthetic Ni-free and Ni-bearing siderites, and comparison to the siderite structure from Graf (1961). Fits were performed in *k*-space on the Fourier-filtered data within the 0-4.5 Å R-range, uncorrected for phase shift (Fig. 5). Standard errors for R and N are estimated to be ±0.03 Å and ± 25%, respectively.

Table 3. Values of the parameters used to fit the Fe and Ni K-edge experimental EXAFS spectra of the synthetic Ni-free and Ni-bearing siderites with the Feff-calculated EXAFS spectra.

Table 4. Proportions of different Ni-bearing phases in the regolith as a function of depth estimated from LC-LS fits of the Ni K-edge EXAFS spectra using EXAFS spectra of different Ni-bearing model compounds.

Table 5. Cell parameters calculated from Rietveld refinement of powder XRD patterns. Results for the synthetic Ni-bearing and Ni-free siderites are compared to a natural sample from 36.1 m in the regolith. The cell parameters from Graf (1961) were used as starting model. Unit cell parameters were refined in space group *R*-3*c* (hexagonal). Mean Coherent Domain (MCD) dimensions were estimated from the Scherrer formula using a Voigt line profile and assuming an isotropic model. Strain parameters and overall Debye-Waller parameters were also refined (data not shown).

SUPPORTING INFORMATION

See the attached document.

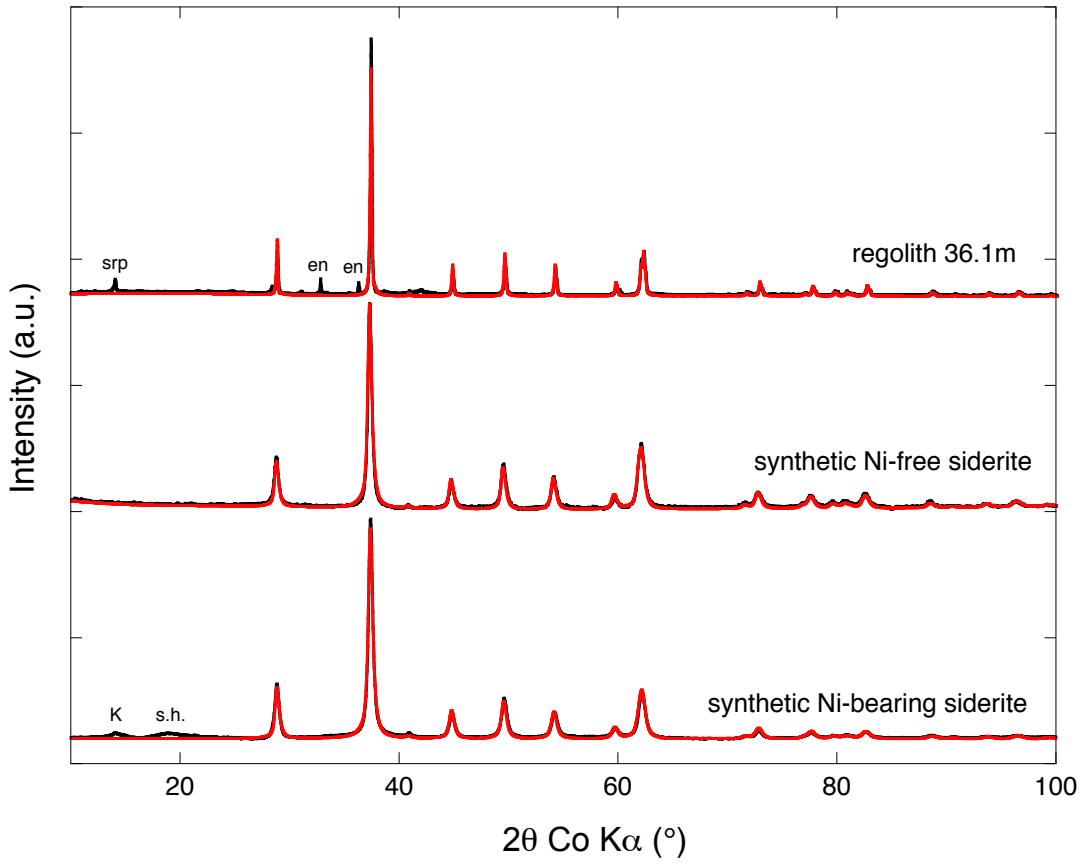

Figure 1. Experimental (black lines) and Rietveld refined (red lines) XRD patterns of the synthetic Ni-free and Ni-bearing siderites. srp: serpentine, en: enstatite. The "K" at low angles above the XRD pattern of the Ni-bearing siderite indicates a diffraction peak from the Kapton foil of the anoxic cell and the label "s.h." indicates scattering from the sample holder.

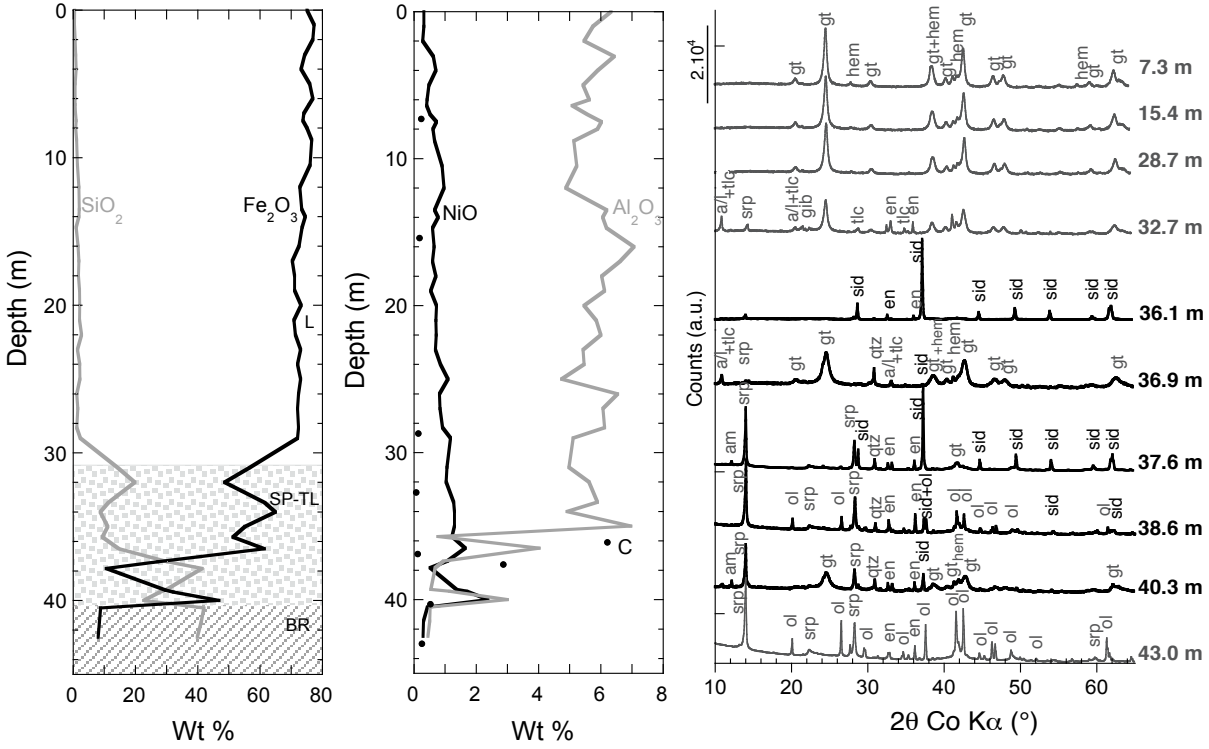

Figure 2. SiO_2, Fe_2O_3, NiO, Al_2O_3 and C concentrations and XRD patterns of the samples collected as a function of depth in the regolith. BR: bedrock (dashed area); SP-TL: alternating saprolite and transition-laterite (dotted area); L: laterite; a: asbolane; l: lithiophorite; am: amphibole; srp: serpentine; tlc: talc; gt: goethite; hem: hematite; chr: chromite; sid: siderite; qtz: quartz. XRD patterns of the samples containing siderite are shown in black and occur at depths from 36.1 m to 40.3 m.

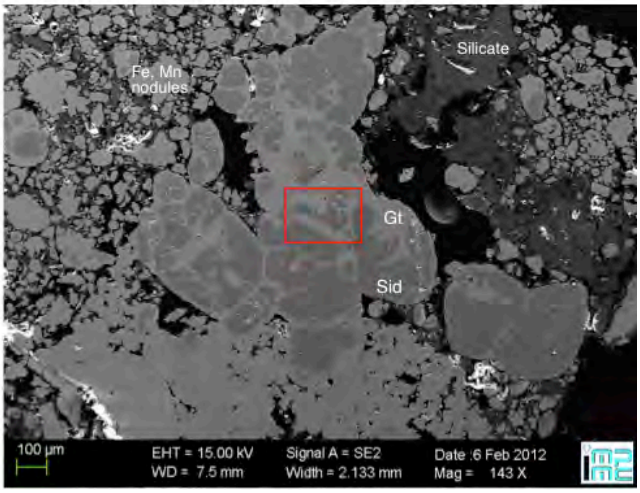

Figure 3. SEM secondary electron image of siderite grains about 200 µm in diameter (dark gray, e.g. "Sid") aggregated in grape-like clusters in the sample collected at 36 m depth in the regolith. The pale gray color corresponds to goethite (e.g. "Gt"). The red square corresponds to the location of the compositional analyses in Figure 4.

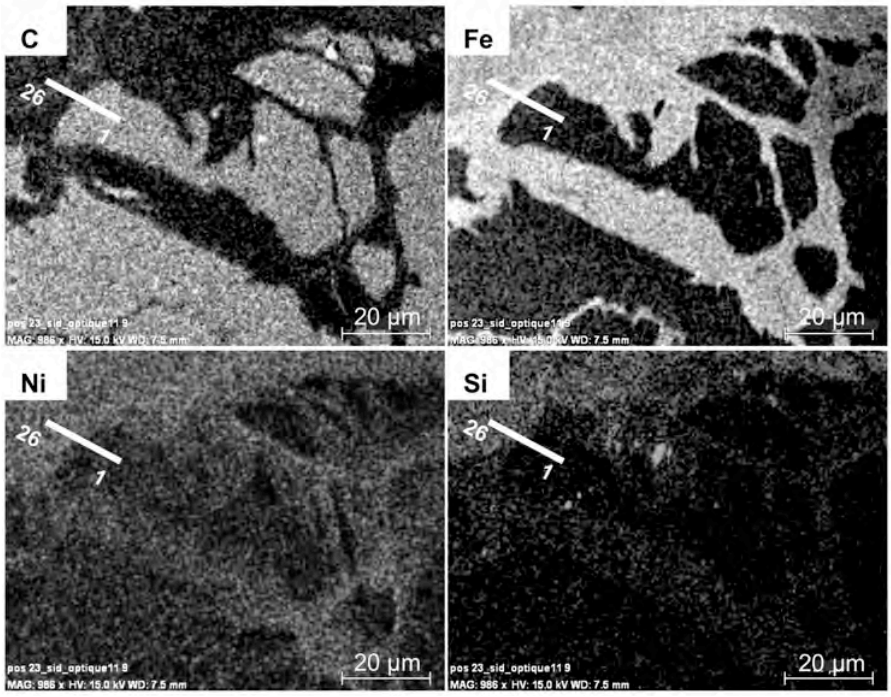

Figure 4. SEM-EDX chemical distribution of carbon, iron, nickel, and silicon showing siderite (high carbon content) embedded in a matrix of Fe-oxides and Mg-silicates in the sample collected at 36.1 m depth in the regolith. The bold white line shows the location of the EPMA analyzes reported in Tables 1 and S2.

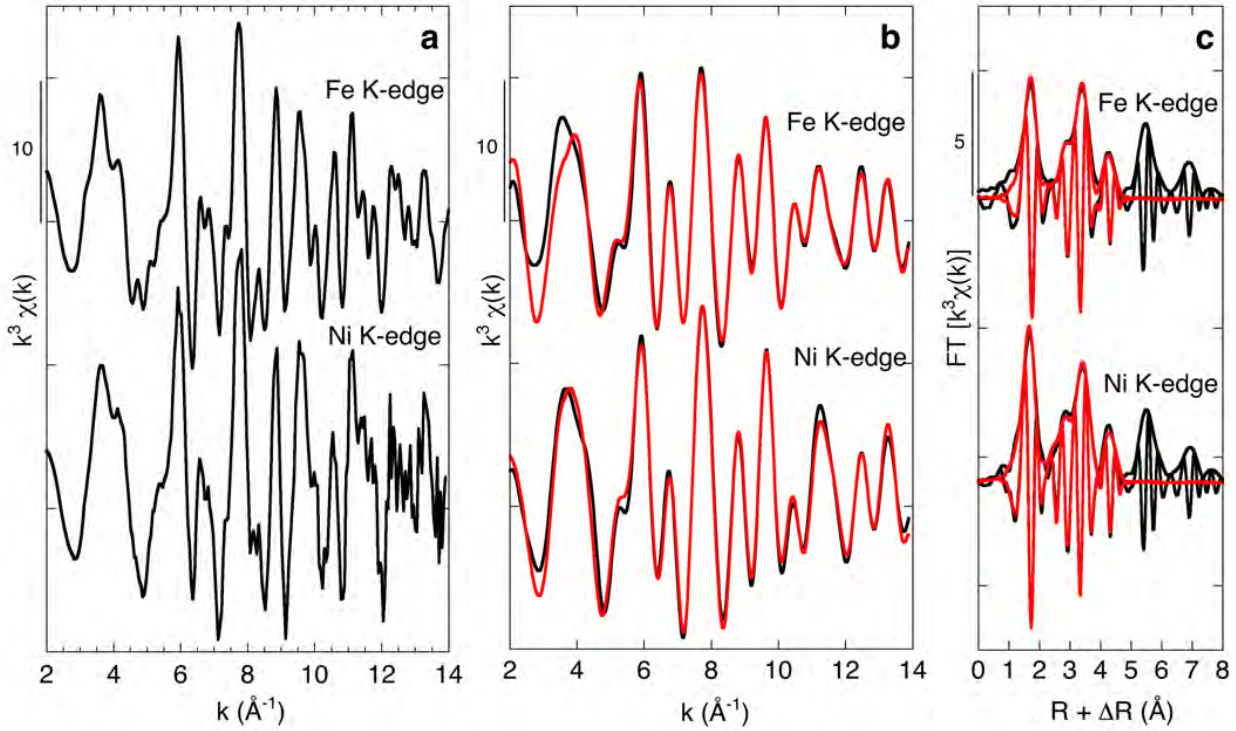

Figure 5. Comparison of the Fe and Ni K-edge EXAFS data of the Ni-free and Ni-bearing synthetic samples, respectively. The a panel shows the background-subtracted, k^3-weighted EXAFS spectra, and the b panel shows fits of the Fourier-filtered backtransformed EXAFS spectra over the R-range 0 - 4.5 Å. Panel c shows the shell-by-shell fit within the 0 - 4.5 Å R-range, uncorrected for phase-shift. Black and red lines correspond to experimental data and shell-by-shell fits, respectively.

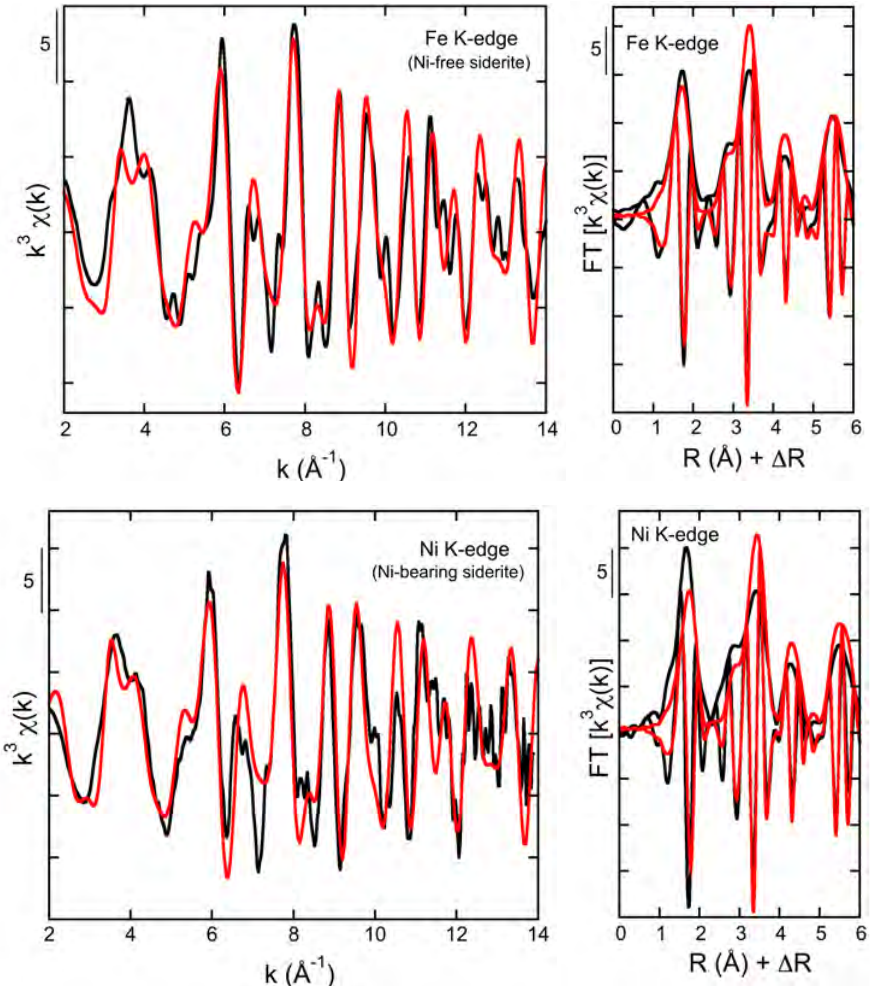

Figure 6. (Left panels) Fits of the Fe and Ni K-edge experimental EXAFS spectra of the synthetic Ni-free and Ni-bearing siderites (black lines) with the Feff-calculated EXAFS spectra (red lines) obtained by including the parameters σ, S_0^2 and ΔE_O; (Right panels) the corresponding Fourier Transforms of the EXAFS spectra.

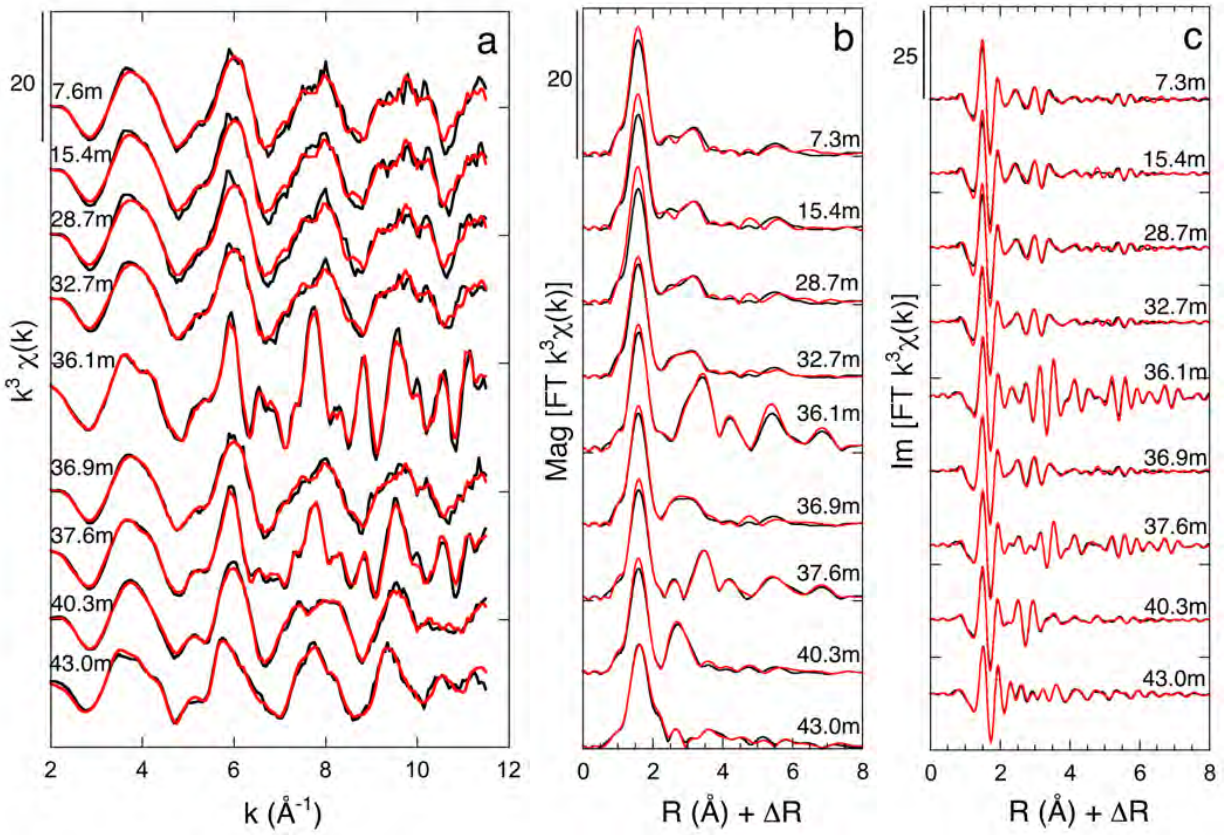

Figure 7. Ni K-edge (a) EXAFS spectra and corresponding (b) FT (real part), and (c) FT (imaginary part) for samples collected at various depths in the lateritic regolith. Black lines correspond to experimental data and red lines correspond to linear combination least squares fits (see Table 4 for quantitative results).

TABLES

Table 1. EPMA analyses at the interface between the siderite grain and its surrounding matrix of Fe-oxides and Mg-silicates shown in Figure 3.

Wt%	FeO	MnO	NiO	CoO	MgO	SiO_2	TOTAL[(1)]	MgO/SiO_2
Siderite								
Mean (n=12)[(2)]	*54.14*	*3.91*	*0.86*	*0.40*	*0.94*	*0.03*	*60.36*	*31*
St dev	1.45	0.44	0.15	0.07	0.11	0.04	1.25	
Goethite								
Mean (n=13)[(2)]	*66.53*	*5.58*	*1.93*	*0.92*	*0.67*	*0.56*	*76.23*	*1.2*
St dev	*2.01*	*1.31*	*0.17*	*0.13*	*0.11*	*0.19*	*0.93*	

(1): Ca, K, Al, and Cr also detected by EPMA at trace levels (< 0.10 wt%) are not included.

(2): See Supporting Information for details on these analyses

Table 2. Results of shell-by-shell fit of the Ni and Fe K-edges EXAFS spectra for the synthetic Ni-free and Ni-bearing siderites, and comparison to the siderite structure from Graf (1961). Fits were performed in *k*-space on the Fourier-filtered data within the 0 to 4.5 Å R-range, uncorrected for phase shift (Figure 5).

EXAFS spectrum	*R* (Å) [1]	*N* [2]	σ (Å) [3]	ΔE_0 (eV) [4]	*NSSR* [5]
Synthetic Ni-bearing	2.08	5.8 Ni-O	0.07	+10.8	0.030
siderite @ Ni K-edge	2.97	6.8 Ni-C	-	-	
	3.25	4.5 Ni-O	-	-	
	3.70	4.7 Ni-Fe	-	-	
	4.05	7.5 Ni-O	-	-	
	4.68	4.5 Ni-Fe	-	-	
Synthetic Ni-free	2.13	5.1 Fe-O	0.07	+11.7	0.011
siderite @ Fe K-edge	3.01	4.8 Fe-C	-	-	
	3.27	4.5 Fe-O		-	
	3.73	5.3 Fe-Fe	-	-	
	4.08	5.1 Fe-O	-	-	
	4.67	4.7 Fe-Fe	-	-	
			-		
Siderite structure	2.14	6.0 Fe-O			
(Graf, 1961)	2.99	6.0 Fe-C			
	3.25	6.0 Fe-O			
	3.72	6.0 Fe-Fe			
	3.84	2.0 Fe-C			
	4.05	6.0 Fe-O			
	4.08	6.0 Fe-O			
	4.53	6.0 Fe-O			
	4.69	6.0 Fe-Fe			

[1] R is the interatomic distance (estimated accuracy is ± 0.03 Å). [2] N is the EXAFS-derived coordination number (± 25%). [3] σ(Å) is the Debbye-Waller factor (± 0.01 Å). [4] ΔE_0 values are the energy shift referenced to the metallic Ni (± 1 eV).
[5] Normalized Sum of Square Residual (NSSR) calculated as $\Sigma(k^3\chi_{exp} - k^3\chi_{fit})^2/\Sigma(k^3\chi_{exp})^2$

Table 3. Values of the parameters used to fit the Fe and Ni K-edge experimental EXAFS spectra of the synthetic Ni-free and Ni-bearing siderites with the Feff-calculated EXAFS spectra.

Sample	σ (Å)	S_0^2	ΔE_0 (eV)	Sum*
Ni-siderite	0.069	0.856	14.3	3136
Fe-siderite	0.068	0.817	11.1	1977

*Sum: $\Sigma_{i=1,n} (k^3\chi_{fit} - k^3\chi_{exp})^2$ (where n is the number of points in the spectra)

Table 4. Proportions of different Ni-bearing phases in the regolith as a function of depth estimated from LC-LS fits of the Ni K-edge EXAFS spectra using EXAFS spectra of different Ni-bearing model compounds.

Sample	Ni-siderite	Ni-goethite	Ni-bearing Asb/Lit	Ni-rich serpentine	Ni-poor serpentine	Ni-forsterite	NSSR [(1)]
7.3 m	---	80	20	---	---	---	0.160
15.4 m	---	82	18	---	---	---	0.146
28.7 m	---	75	25	---	---	---	0.152
32.7 m	---	68	23	9	---	---	0.178
36.1 m	88	---	---	12	---	---	0.082
36.9 m	---	66	19	---	15	---	0.117
37.6 m	52	---	---	48	---	---	0.089
40.3 m	---	48	---	52	---	---	0.066
43.0 m	---	---	---	---	42	58	0.219

[(1)] Calculated as $\Sigma(k^3\chi_{exp} - k^3\chi_{fit})^2/\Sigma(k^3\chi_{exp})^2$

Table 5. Cell parameters calculated from Rietveld refinement of powder XRD patterns. Results for the synthetic Ni-bearing and Ni-free siderites are compared to a natural sample from 36.1 m in the regolith. The cell parameters from Graf (1961) were used as starting model. Unit cell parameters were refined in space group *R*-3*c* (hexagonal). Mean Coherent Domain (MCD) dimensions were estimated from the Scherrer formula using a Voigt line profile and assuming an isotropic model. Strain parameters and overall Debye-Waller parameters were also refined (data not shown).

Sample	*a* (nm)	*c* (nm)	MCD[111] (nm)
Ni-siderite	0.469(2)	1.53(1)	27(2)
Ni-free siderite	0.469(2)	1.54(1)	30(5)
Laterite 36.1 m	0.469(1)	1.537(5)	100(50)
Siderite (Graf, 1961)	0.4689	1.537	-